Available online at www.sciencedirect.com
ScienceDirect
International Journal of Thermal Sciences 46 (2007) 1104–1111
International Journal of Thermal Sciences
www.elsevier.com/locate/ijts

Slip flow in elliptic microchannels

Zhipeng Duan *, Y.S. Muzychka

Faculty of Engineering and Applied Science, Memorial University of Newfoundland, St. John's, NL, A1B 3X5, Canada

Received 17 September 2006; received in revised form 27 January 2007; accepted 28 January 2007

Available online 26 March 2007

Abstract

Microscale fluid dynamics has received intensive interest due to the emergence of Micro-Electro-Mechanical Systems (MEMS) technology. When the mean free path of the gas is comparable to the channel's characteristic dimension, the continuum assumption is no longer valid and a velocity slip may occur at the duct walls. The elliptic cross-section is one useful channel shape that may be produced by microfabrication. The elliptic microchannels have potential practical applications in MEMS. Slip flow in elliptic microchannels has been examined and a detailed theoretical analysis has been performed. A solution is obtained using elliptic cylinder coordinates and the separation of variables method. A simple model is developed for predicting the Poiseuille number in elliptic microchannels for slip flow. The developed model may be used to predict mass flow rate and pressure distribution of slip flow in elliptic microchannels.

Keywords: Slip flow; Elliptic microchannels; Pressure distribution

1. Introduction

Fluid flow in microchannels has emerged as an important area of research. This has been motivated by their various applications such as medical and biomedical use, computer chips, and chemical separations. The advent of Micro-Electro-Mechanical Systems (MEMS) has opened up a new research area where non-continuum behavior is important. MEMS are one of the major advances of industrial technologies in the past decades. MEMS refer to devices which have a characteristic length of less than 1 mm but greater than 1 μm, which combine electrical and mechanical components and which are fabricated using integrated circuit fabrication technologies. Micron-size mechanical and biochemical devices are becoming more prevalent both in commercial applications and in scientific research.

Microchannels are the fundamental part of microfluidic systems. In addition to connecting different devices, microchannels are also utilized as biochemical reaction chambers, in physical particle separation, in inkjet print heads, in infrared detectors, in diode lasers, in miniature gas chromatographs, or as heat exchangers for cooling computer chips. Understanding the flow characteristics of microchannel flows is very important in determining pressure distribution, heat transfer, and transport properties of the flow. The characteristic dimension associated with the term "microchannels" is ambiguous. Nominally, microchannels may be defined as channels whose characteristic dimensions are from one micron to one millimeter. Typical applications may involve characteristic dimensions in the range of approximately 10 to 200 μm. Generally, above one millimeter the flow exhibits behavior which is the same as continuum flows. The elliptic cross-section is one useful channel shape that may be produced by microfabrication. The elliptic cross-section has potential practical applications in MEMS.

The Knudsen number (Kn) relates the molecular mean free path of gas to a characteristic dimension of the duct. Knudsen number is very small for continuum flows. However, for microscale gas flows where the gas mean free path becomes comparable with the characteristic dimension of the duct, the Knudsen number may be greater than 10^{-3}. Microchannels with characteristic lengths on the order of 100 μm would produce flows inside the slip regime for gas with a typical mean free path of approximately 100 nm at standard conditions. The slip flow regime to be studied here is classified as $10^{-3} < Kn < 10^{-1}$.

* Corresponding author. Tel.: +1 709 7378809; fax: +1 709 7374042.
E-mail address: zpduan@engr.mun.ca (Z. Duan).

1290-0729/$ – see front matter
doi:10.1016/j.ijthermalsci.2007.01.026

Nomenclature

A	area of ellipse	m^2
a	major semi-axis of ellipses	m
b	minor semi-axis of ellipses	m
c	half focal length of ellipses	m
D_h	hydraulic diameter, $= 4A/P$	
ds_1, ds_2	elemental distance for elliptic cylinder coordinate system	m
e	eccentricity, $= \sqrt{1 - b^2/a^2}$	
$E(e)$	complete elliptical integral of the second kind	
F	η-dependent velocity function	
f	Fanning friction factor, $= \tau/(\frac{1}{2}\rho\bar{u}^2)$	
G	ψ-dependent velocity function	
g_1, g_2, g_3	metric coefficients	
Kn	Knudsen number, $= \lambda/D_h$	
Kn^*	modified Knudsen number, $= Kn(2-\sigma)/\sigma$	
L	channel length	m
L^+	dimensionless channel length, $= L/D_h\,Re_{D_h}$	
Ma	Mach number, $= u/V_s$	
$\dot{m}$	mass flow rate	kg/s
Po	Poiseuille number, $= \bar{\tau}D_h/\mu\bar{u}$	
P	perimeter of ellipses	m
p	pressure	N/m^2
R	specific gas constant	J/kg K
Re	Reynolds number, $= D_h\bar{u}/\nu$	
T	temperature	K
U	velocity scale	m/s
u	fluid velocity component in z direction	m/s
$\bar{u}$	average velocity	m/s
V_s	speed of sound, $= \sqrt{\gamma RT}$	
x, y	Cartesian coordinates coinciding with axes of ellipse	m
z	coordinate in flow direction	m

Greek symbols

α	constants	
γ	ratio of specific heats	
δ	eigenvalue	
ε	aspect ratio, $= b/a$	
η, ψ, z	elliptic cylinder coordinates	
η_0	parameter of elliptic cylinder coordinates	
λ	molecular mean free path	m
μ	dynamic viscosity	Ns/m^2
ν	kinematic viscosity	m^2/s
ρ	gas density	kg/m^3
σ	tangential momentum accommodation coefficient	
τ	wall shear stress	N/m^2
ϕ	η, ψ-dependent velocity function	

Subscripts

c	continuum
i	inlet
o	outlet

2. Literature review

When the molecular mean free path is comparable to the channel's characteristic dimension, the continuum assumption is no longer valid and the gas exhibits non-continuum effects such as velocity slip and temperature jump at the channel walls. Traditional examples of non-continuum gas flows in channels include low-density applications such as high-altitude aircraft or vacuum technology. The recent development of microscale fluid systems has motivated great interest in this field of study. Microfluidic systems must take into account non-continuum effects. There is strong evidence to support the use of Navier–Stokes and energy equations to model the slip flow problem, while the boundary conditions are modified by including velocity slip and temperature jump at the channel walls [1–4].

The small length scales commonly encountered in microfluidic devices suggest that rarefaction effects are important. For example, experiments conducted by Arkilic et al. [2,3], Liu et al. [4], Pfalher et al. [5,6], Harley et al. [7], Choi et al. [8], Wu et al. [9], Araki et al. [10] on the transport of gases in microchannels confirm that continuum analyses are unable to predict flow properties in micro-sized devices.

Arkilic et al. [2,3] investigated helium flow through microchannels. The microchannels were 52.25 μm wide, 1.33 μm deep, 7.5 mm long. The results showed that the pressure drop over the channel length was less than the continuum flow results. The friction coefficient was only about 40% of the theoretical values. The significant reduction in the friction coefficient may be due to the slip flow regime, as according to the flow regime classification by Schaaf and Chambre [11], the flows studied by Arkilic et al. [2,3] are mostly within the slip flow regime, only bordering the transition regime near the outlet. When using the Navier–Stokes equations with slip flow boundary conditions, the model was able to predict the flow accurately.

Liu et al. [4] has also proven that the solution to the Navier–Stokes equation combined with slip flow boundary conditions show good agreement with the experimental data in microchannel flows.

Araki et al. [10] investigated frictional characteristics of nitrogen and helium flows through three different trapezoidal microchannels whose hydraulic diameter is from 3 to 10 μm. The measured friction factor was smaller than that predicted by the conventional theory. They concluded that this deviation was caused by the rarefaction effects.

The analytical study of internal flows with slip previously has been confined to simple geometries. Kennard [12] studied internal flows with slip in the circular tube and parallel-plate channel. Ebert and Sparrow [13] performed an analysis to determine the velocity and pressure drop characteristics of slip flow in rectangular and annular ducts.

Sreekanth [14] developed a second-order analytical model for slip flow in circular tubes and Mitsuya [15] proposed a second-order analytical model for parallel plates. Aubert and Colin [16] studied slip flow in rectangular microchannels using the second-order boundary conditions proposed by Deissler [17]. In a later study, Colin et al. [18] presented experimental results for nitrogen and helium flows in a series of silicon rectangular microchannels. The authors proposed that the second-order slip flow model is valid for Knudsen numbers up to about 0.25.

A variety of researchers have attempted to develop second-order slip models which can be used in the transition regime. However, there are large variations in the second-order slip coefficient. The lack of a universally accepted second-order slip coefficient is a major problem in extending Navier–Stokes equations into the transition regime [19]. As analytical models derived using the first-order slip boundary condition have been shown to relatively accurate up to Knudsen numbers of approximately 0.1 [19], the first-order slip boundary condition will be employed in this paper.

3. Theoretical analysis

Using the method of scale analysis, we examine the momentum equation and consider the various force balances. Considering the force balance between the friction and pressure forces for a long microchannel:

$$\frac{\Delta p}{L} \sim \frac{\mu U}{D_h^2}$$

then, the incompressible flow criterion for microchannel flows can be obtained:

$$\frac{\Delta p}{p} = \frac{\Delta \rho}{\rho} \sim \frac{\mu U L}{\rho R T D_h^2} \sim \frac{L\,Ma^2}{D_h\,Re_{D_h}} \sim \frac{L}{D_h} Kn^2\,Re_{D_h} \ll 1$$

where we have employed ideal gas equation of state $p = \rho RT$ and $Kn \approx Ma/Re$ and assumed that the flow is isothermal. As the pressure drop is owing to viscous effects and not to any free expansion of the gas, the isothermal assumption should be reasonable. Therefore, in microchannel flows which are dominated by viscous effects, density changes may be significant even though the Mach number is very small. The gas flow through a microchannel can be considered incompressible when the Reynolds number is very low with comparatively high Knudsen numbers or the Knudsen number is small with moderate Reynolds numbers.

Comparing the scale between friction and inertial forces to obtain the following relation:

$$\frac{\mu \frac{\partial^2 u}{\partial y^2}}{\rho u \frac{\partial u}{\partial x}} \sim \frac{\mu \frac{U}{D_h^2}}{\frac{\rho U^2}{L}} = \frac{L}{D_h\,Re_{D_h}} = L^+$$

A schematic diagram of the elliptic cross-section with coordinates and other dimensional nomenclature is showed in Fig. 1. The starting point of the analysis is the law of conservation

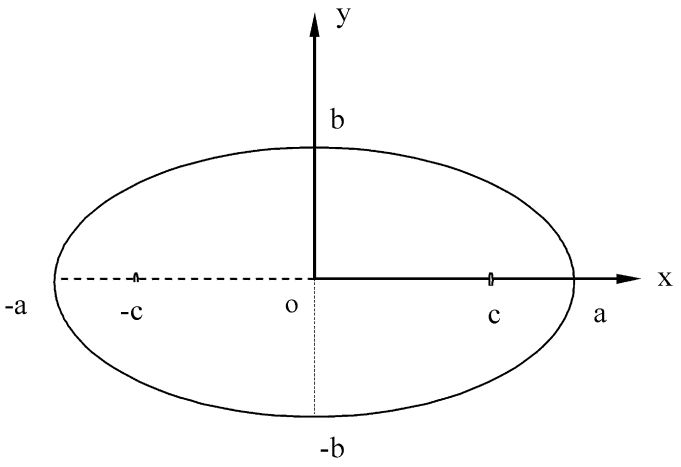

Fig. 1. An elliptic duct.

of momentum. When $L^+ \gg 1$, the continuum flow momentum equation reduces to the form

$$\frac{\partial^2 u}{\partial x^2} + \frac{\partial^2 u}{\partial y^2} = \frac{1}{\mu}\frac{\mathrm{d}p}{\mathrm{d}z} \tag{1}$$

It is convenient to use elliptic cylinder coordinates [20,21] to facilitate the solution process. The metric coefficients for this system of coordinates are

$$g_1 = g_2 = c^2\left(\cosh^2\eta - \cos^2\psi\right) \tag{2}$$

$$g_3 = 1 \tag{3}$$

The elemental distance for this coordinate system is [20,21]

$$\mathrm{d}s_1 = c\left(\cosh^2\eta - \cos^2\psi\right)^{1/2}\mathrm{d}\eta \tag{4}$$

$$\mathrm{d}s_2 = c\left(\cosh^2\eta - \cos^2\psi\right)^{1/2}\mathrm{d}\psi \tag{5}$$

In elliptic cylinder coordinates, the momentum equation becomes

$$\frac{\partial^2 u}{\partial \eta^2} + \frac{\partial^2 u}{\partial \psi^2} = \frac{c^2}{\mu}\frac{\mathrm{d}p}{\mathrm{d}z}\left(\cosh^2\eta - \cos^2\psi\right) \tag{6}$$

The velocity distribution must satisfy the slip boundary condition at the walls. The local slip velocity is proportional to the local velocity gradient normal to the wall. In elliptic cylinder coordinates, the boundary conditions assuming a one quarter basic cell, are:

$$\frac{1}{\sqrt{g_2}}\frac{\partial u}{\partial \psi} = 0 \quad \text{at } \psi = 0 \tag{7}$$

$$\frac{1}{\sqrt{g_2}}\frac{\partial u}{\partial \psi} = 0 \quad \text{at } \psi = \frac{\pi}{2} \tag{8}$$

$$\frac{1}{\sqrt{g_1}}\frac{\partial u}{\partial \eta} = 0 \quad \text{at } \eta = 0 \tag{9}$$

$$u = -\frac{\lambda\frac{2-\sigma}{\sigma}}{\sqrt{g_1}}\frac{\partial u}{\partial \eta} \quad \text{at } \eta = \eta_0 \tag{10}$$

where λ is the molecular mean free path. The constant σ denotes tangential momentum accommodation coefficient, which has values that typically lie between 0.87 and 1 [22]. Although

the nature of the tangential momentum accommodation coefficients is still an active research problem, almost all evidence indicates that for most gas–solid interactions the coefficients are approximately 1.0. The same procedure is valid even if $\sigma \neq 1$, defining a modified Knudsen number as $Kn^* = Kn(2-\sigma)/\sigma$.

The parameter η_0 is related to the major and minor axes through

$$\eta_0 = \ln \frac{1 + b/a}{\sqrt{1-(b/a)^2}} \tag{11}$$

The half focal length of ellipses c is defined such that

$$c = \frac{a}{\cosh \eta_0} = \frac{b}{\sinh \eta_0} \tag{12}$$

Eq. (6) may be solved using the separation of variables method [20], assuming that

$$u(\eta, \psi) = \phi(\eta, \psi) + F(\eta) + G(\psi) \tag{13}$$

After differentiating twice with respect to η and ψ we get

$$\begin{aligned} \frac{\partial^2 u}{\partial \eta^2} &= \frac{\partial^2 \phi}{\partial \eta^2} + \frac{\partial^2 F}{\partial \eta^2} \\ \frac{\partial^2 u}{\partial \psi^2} &= \frac{\partial^2 \phi}{\partial \psi^2} + \frac{\partial^2 G}{\partial \psi^2} \end{aligned} \tag{14}$$

Substitution of Eq. (14) into Eq. (6) gives

$$\frac{\partial^2 \phi}{\partial \eta^2} + \frac{\partial^2 \phi}{\partial \psi^2} + \frac{\partial^2 F}{\partial \eta^2} + \frac{\partial^2 G}{\partial \psi^2} = \frac{c^2}{\mu}\frac{\mathrm{d}p}{\mathrm{d}z}\left(\cosh^2 \eta - \cos^2 \psi\right) \tag{15}$$

Laplace's equation, $\nabla^2 \phi = 0$, can be obtained by letting

$$\begin{aligned} \frac{\partial^2 F}{\partial \eta^2} &= \frac{c^2}{2\mu}\frac{\mathrm{d}p}{\mathrm{d}z}\cosh 2\eta \\ \frac{\partial^2 G}{\partial \psi^2} &= -\frac{c^2}{2\mu}\frac{\mathrm{d}p}{\mathrm{d}z}\cos 2\psi \end{aligned} \tag{16}$$

Integrating both expressions of Eq. (16) twice yields the following substitutions for $F(\eta)$ and $G(\psi)$:

$$\begin{aligned} F(\eta) &= \frac{c^2}{8\mu}\frac{\mathrm{d}p}{\mathrm{d}z}\cosh 2\eta \\ G(\psi) &= \frac{c^2}{8\mu}\frac{\mathrm{d}p}{\mathrm{d}z}\cos 2\psi \end{aligned} \tag{17}$$

After applying separation of variables to $\phi(\eta, \psi)$, the solution of the Laplace equation is

$$\begin{aligned} \phi(\eta, \psi) = &\left[A\cos(\delta\psi) + B\sin(\delta\psi)\right] \\ &\times \left[C\cosh(\delta\eta) + D\sinh(\delta\eta)\right] \end{aligned} \tag{18}$$

The solution for $u(\eta, \psi)$ is the sum of the solution of the Laplace equation, $\nabla^2 \phi = 0$, and of Eq. (17); therefore we have

$$\begin{aligned} u = &\left[A\cos(\delta\psi) + B\sin(\delta\psi)\right]\left[C\cosh(\delta\eta) + D\sinh(\delta\eta)\right] \\ &+ \frac{c^2}{8\mu}\frac{\mathrm{d}p}{\mathrm{d}z}(\cosh 2\eta + \cos 2\psi) \end{aligned} \tag{19}$$

According to the boundary condition, Eq. (7)

$$B = 0$$

In terms of the boundary condition, Eq. (9)

$$D = 0$$

From the boundary condition, Eq. (8)

$$\delta_n = n, \quad n = 0, 2, 4, 6, \ldots \text{ (even)}$$

in which the δ_n are a set of eigenvalues. Therefore, the solution of this problem becomes

$$\begin{aligned} u = &\sum_{n=0,\text{even}}^{\infty} C_n' \cos(n\psi)\cosh(n\eta) \\ &+ \frac{c^2}{8\mu}\frac{\mathrm{d}p}{\mathrm{d}z}(\cosh 2\eta + \cos 2\psi) \end{aligned} \tag{20}$$

and

$$\frac{\partial u}{\partial \eta} = \sum_{n=1}^{\infty} C_n' n\cos(n\psi)\sinh(n\eta) + \frac{c^2}{8\mu}\frac{\mathrm{d}p}{\mathrm{d}z}2\sinh 2\eta$$

Applying the final boundary condition, Eq. (10)

$$\begin{aligned} &\sum_{n=0,\text{even}}^{\infty} C_n' \cos(n\psi)\left[\cosh(n\eta_0) \right. \\ &\qquad \left. + \frac{\lambda\frac{2-\sigma}{\sigma}}{c(\cosh^2\eta_0 - \cos^2\psi)^{1/2}} n\sinh(n\eta_0)\right] \\ &= -\frac{c^2}{8\mu}\frac{\mathrm{d}p}{\mathrm{d}z}\left(\cosh 2\eta_0 + \cos 2\psi \right. \\ &\qquad \left. + 2\frac{\lambda\frac{2-\sigma}{\sigma}}{c(\cosh^2\eta_0 - \cos^2\psi)^{1/2}}\sinh(2\eta_0)\right) \end{aligned}$$

a solution for C_n' may be obtained by means of a Fourier expansion.

In order to overcome the difficulty caused by the metric coefficient, we use a binomial series to approximate the metric coefficient and take the first three terms:

$$\begin{aligned} &(1+x)^a = 1 + \sum_{n=1}^{\infty} \frac{a(a-1)(a-2)\cdots(a-n+1)}{n!}x^n \\ &-1 < x < 1 \end{aligned}$$

The metric coefficient may now be written as:

$$\begin{aligned} \frac{1}{\sqrt{g_1}} &= \frac{1}{c(\cosh^2\eta_0 - \cos^2\psi)^{1/2}} = \frac{1}{c\cosh(\eta_0)(1 - \frac{\cos^2\psi}{\cosh^2\eta_0})^{1/2}} \\ &\approx \frac{1 + \frac{1}{2}\frac{\cos^2\psi}{\cosh^2\eta_0} + \frac{3}{8}\frac{\cos^4\psi}{\cosh^4\eta_0}}{c\cosh(\eta_0)} \end{aligned} \tag{21}$$

assuming a three term expansion.

From orthogonality principles, we get

$$\begin{aligned} C_n' = \left\{\int_0^{2\pi} -\frac{c^2}{8\mu}\frac{\mathrm{d}p}{\mathrm{d}z}\right. &\left[\cosh 2\eta_0 + \cos 2\psi \right. \\ &\left. \left. + 2\lambda\frac{2-\sigma}{\sigma}\frac{1 + \frac{1}{2}\frac{\cos^2\psi}{\cosh^2\eta_0} + \frac{3}{8}\frac{\cos^4\psi}{\cosh^4\eta_0}}{c\cosh(\eta_0)}\sinh(2\eta_0)\right]\cos(n\psi)\,\mathrm{d}\psi\right\} \end{aligned}$$

$$\Bigg/\left\{\int_0^{2\pi}\left[\cosh(n\eta_0)+\lambda\frac{2-\sigma}{\sigma}\frac{1+\frac{1}{2}\frac{\cos^2\psi}{\cosh^2\eta_0}+\frac{3}{8}\frac{\cos^4\psi}{\cosh^4\eta_0}}{c\cosh(\eta_0)}n\times\sinh(n\eta_0)\right]\cos^2(n\psi)\,\mathrm{d}\psi\right\}$$

and

$$C_0'=-\frac{c^2}{8\mu}\frac{\mathrm{d}p}{\mathrm{d}z}\left[\cosh 2\eta_0+2\lambda\frac{2-\sigma}{\sigma}\frac{1+\frac{1}{4\cosh^2\eta_0}+\frac{9}{64\cosh^4\eta_0}}{c\cosh(\eta_0)}\sinh(2\eta_0)\right]$$

$$C_2'=-\frac{c^2}{8\mu}\frac{\mathrm{d}p}{\mathrm{d}z}\frac{1+2\lambda\frac{2-\sigma}{\sigma}[\frac{1}{4c\cosh^3(\eta_0)}+\frac{3}{16c\cosh^5(\eta_0)}]\sinh(2\eta_0)}{\cosh(2\eta_0)+2\lambda\frac{2-\sigma}{\sigma}\frac{1+\frac{1}{4\cosh^2\eta_0}+\frac{21}{128\cosh^4\eta_0}}{c\cosh(\eta_0)}\sinh(2\eta_0)}$$

$$C_4'=-\frac{c^2}{8\mu}\frac{\mathrm{d}p}{\mathrm{d}z}\frac{\lambda\frac{2-\sigma}{\sigma}\frac{3}{32c\cosh^5(\eta_0)}\sinh(2\eta_0)}{\cosh(4\eta_0)+4\lambda\frac{2-\sigma}{\sigma}\frac{1+\frac{1}{4\cosh^2\eta_0}+\frac{9}{64\cosh^4\eta_0}}{c\cosh(\eta_0)}\sinh(4\eta_0)}$$

$$C_6'=C_8'=C_{10}'=\cdots=0$$

The solution of this problem becomes:

$$\begin{aligned}u=&-\frac{c^2}{8\mu}\frac{\mathrm{d}p}{\mathrm{d}z}\left[\cosh 2\eta_0+2\lambda\frac{2-\sigma}{\sigma}\frac{1+\frac{1}{4\cosh^2\eta_0}+\frac{9}{64\cosh^4\eta_0}}{c\cosh(\eta_0)}\times\sinh(2\eta_0)\right]\\&-\frac{c^2}{8\mu}\frac{\mathrm{d}p}{\mathrm{d}z}\frac{1+2\lambda\frac{2-\sigma}{\sigma}[\frac{1}{4c\cosh^3(\eta_0)}+\frac{3}{16c\cosh^5(\eta_0)}]\sinh(2\eta_0)}{\cosh(2\eta_0)+2\lambda\frac{2-\sigma}{\sigma}\frac{1+\frac{1}{4\cosh^2\eta_0}+\frac{21}{128\cosh^4\eta_0}}{c\cosh(\eta_0)}\sinh(2\eta_0)}\times\cos(2\psi)\cosh(2\eta)\\&-\frac{c^2}{8\mu}\frac{\mathrm{d}p}{\mathrm{d}z}\frac{\lambda\frac{2-\sigma}{\sigma}\frac{3}{32c\cosh^5(\eta_0)}\sinh(2\eta_0)}{\cosh(4\eta_0)+4\lambda\frac{2-\sigma}{\sigma}\frac{1+\frac{1}{4\cosh^2\eta_0}+\frac{9}{64\cosh^4\eta_0}}{c\cosh(\eta_0)}\sinh(4\eta_0)}\times\cos(4\psi)\cosh(4\eta)\\&+\frac{c^2}{8\mu}\frac{\mathrm{d}p}{\mathrm{d}z}(\cosh 2\eta+\cos 2\psi)\end{aligned}\tag{22}$$

The eccentricity of the ellipse is defined as:

$$e=\sqrt{1-\left(\frac{b}{a}\right)^2}\tag{23}$$

and the hydraulic diameter as:

$$D_h=\frac{\pi b}{E(e)}\tag{24}$$

where $E(e)$ is the complete elliptical integral of the second kind [23]. The characteristic length scale in the present analysis is defined as the hydraulic diameter ($2b<D_h\leqslant\pi b$), such that:

$$Kn=\frac{\lambda}{D_h}=\frac{\lambda}{\frac{\pi b}{E(e)}}\tag{25}$$

Finally, the velocity distribution is as follows:

$$\begin{aligned}u=&-\frac{c^2}{8\mu}\frac{\mathrm{d}p}{\mathrm{d}z}\left[\cosh 2\eta_0+2\frac{\pi b\,Kn_{D_h}}{E(e)}\frac{2-\sigma}{\sigma}\times\frac{1+\frac{1}{4\cosh^2\eta_0}+\frac{9}{64\cosh^4\eta_0}}{c\cosh(\eta_0)}\sinh(2\eta_0)\right]\\&-\frac{c^2}{8\mu}\frac{\mathrm{d}p}{\mathrm{d}z}\left\{1+2\frac{\pi b\,Kn_{D_h}}{E(e)}\frac{2-\sigma}{\sigma}\left[\frac{1}{4c\cosh^3(\eta_0)}+\frac{3}{16c\cosh^5(\eta_0)}\right]\sinh(2\eta_0)\right\}\\&\Bigg/\left\{\cosh(2\eta_0)+2\frac{\pi b\,Kn_{D_h}}{E(e)}\frac{2-\sigma}{\sigma}\times\frac{1+\frac{1}{4\cosh^2\eta_0}+\frac{21}{128\cosh^4\eta_0}}{c\cosh(\eta_0)}\sinh(2\eta_0)\right\}\\&\times\cos(2\psi)\cosh(2\eta)\\&-\frac{c^2}{8\mu}\frac{\mathrm{d}p}{\mathrm{d}z}\left\{\frac{\pi bKn_{D_h}}{E(e)}\frac{2-\sigma}{\sigma}\frac{3}{32c\cosh^5(\eta_0)}\sinh(2\eta_0)\right\}\\&\Bigg/\left\{\cosh(4\eta_0)+4\frac{\pi b\,Kn_{D_h}}{E(e)}\frac{2-\sigma}{\sigma}\times\frac{1+\frac{1}{4\cosh^2\eta_0}+\frac{9}{64\cosh^4\eta_0}}{c\cosh(\eta_0)}\sinh(4\eta_0)\right\}\\&\times\cos(4\psi)\cosh(4\eta)+\frac{c^2}{8\mu}\frac{\mathrm{d}p}{\mathrm{d}z}(\cosh 2\eta+\cos 2\psi)\end{aligned}\tag{26}$$

In the limit of $Kn\to 0$, Eq. (26) reduces to its continuum flow solution [24]:

$$u=-\frac{c^2}{8\mu}\frac{\mathrm{d}p}{\mathrm{d}z}\left[\cosh 2\eta_0+\frac{1}{\cosh 2\eta_0}\cos(2\psi)\cosh(2\eta)-\cosh(2\eta)-\cos(2\psi)\right]\tag{27}$$

The mean velocity is found by integration of Eq. (26) across the section of the duct

$$\begin{aligned}\bar{u}&=\frac{1}{A}\int u\,\mathrm{d}A=\frac{\int u\,\mathrm{d}s_1\,\mathrm{d}s_2}{\int \mathrm{d}s_1\,\mathrm{d}s_2}\\&=\frac{\int_0^{\eta_0}\int_0^{2\pi}uc^2(\cosh^2\eta-\cos^2\psi)\,\mathrm{d}\eta\,\mathrm{d}\psi}{\int_0^{\eta_0}\int_0^{2\pi}c^2(\cosh^2\eta-\cos^2\psi)\,\mathrm{d}\eta\,\mathrm{d}\psi}\\&=\frac{\int_0^{\eta_0}\int_0^{2\pi}uc^2(\cosh^2\eta-\cos^2\psi)\,\mathrm{d}\eta\,\mathrm{d}\psi}{\pi ab}\end{aligned}\tag{28}$$

We can define the Poiseuille number using the above equations:

$$Po_{D_h}=\frac{\bar{\tau}D_h}{\mu\bar{u}}=\frac{(-\frac{A}{P}\frac{\mathrm{d}p}{\mathrm{d}z})D_h}{\mu\bar{u}}=\frac{-\frac{\mathrm{d}p}{\mathrm{d}z}(\frac{\pi b}{E(e)})^2}{4\mu\bar{u}}\tag{29}$$

The solution can be obtained using commercially available algebraic software tools, such as Maple 9 [25]. It can be demonstrated that the limit of Eq. (29) for $b/a\to 1$ corresponds to circular tubes [12]:

$$Po_{D_h}=\frac{8}{1+\frac{2-\sigma}{\sigma}8Kn}\tag{30}$$

Table 1
A comparison of the *Po* using one to four terms of binomial series approximation

ε	Po ($Kn^* = 0.1$)				Po ($Kn^* = 0.01$)			
	1 term	2 terms	3 terms	4 terms	1 term	2 terms	3 terms	4 terms
	1	$1+\frac{1}{2}\frac{\cos^2\psi}{\cosh^2\eta_0}$	$1+\frac{1}{2}\frac{\cos^2\psi}{\cosh^2\eta_0}+\cdots$	$1+\frac{1}{2}\frac{\cos^2\psi}{\cosh^2\eta_0}+\cdots$	1	$1+\frac{1}{2}\frac{\cos^2\psi}{\cosh^2\eta_0}$	$1+\frac{1}{2}\frac{\cos^2\psi}{\cosh^2\eta_0}+\cdots$	$1+\frac{1}{2}\frac{\cos^2\psi}{\cosh^2\eta_0}+\cdots$
0.1	5.03	4.66	4.49	4.38	8.84	8.72	8.66	8.62
0.2	4.96	4.61	4.46	4.36	8.54	8.43	8.38	8.34
0.3	4.91	4.58	4.44	4.36	8.25	8.16	8.11	8.08
0.4	4.86	4.56	4.44	4.37	8.01	7.92	7.88	7.86
0.5	4.82	4.54	4.44	4.39	7.82	7.74	7.71	7.69
0.6	4.77	4.52	4.44	4.41	7.67	7.60	7.58	7.57
0.7	4.70	4.49	4.44	4.42	7.57	7.51	7.50	7.49
0.8	4.63	4.47	4.44	4.43	7.57	7.45	7.44	7.44
0.9	4.54	4.45	4.44	4.44	7.44	7.42	7.42	7.41
1	4.44	4.44	4.44	4.44	7.41	7.41	7.41	7.41

The mass flow rate in the microchannel is given by using the equation of state and assuming $Po = Po_c/(1+\alpha\, Kn^*)$ which is discussed later in this paper:

$$\dot{m} = \rho\bar{u}A = -\frac{\pi ab(\frac{\pi b}{E(e)})^2}{4\mu\, Po_c RT}\frac{\mathrm{d}p}{\mathrm{d}z}\left(p + \alpha\frac{2-\sigma}{\sigma}p\,Kn\right) \tag{31}$$

We can use $p\,Kn = p_o\,Kn_o$ since $p\,Kn$ is constant for isothermal flow. Integrating Eq. (31), we obtain

$$\dot{m} = \rho\bar{u}A = \frac{\pi abp_o^2(\frac{\pi b}{E(e)})^2}{8\mu\, Po_c RTz} \times\left[\frac{p_i^2}{p_o^2} - \frac{p_z^2}{p_o^2} + 2\alpha\frac{2-\sigma}{\sigma}Kn_o\left(\frac{p_i}{p_o} - \frac{p_z}{p_o}\right)\right] \tag{32}$$

Letting $z = L$ gives:

$$\dot{m} = \rho\bar{u}A = \frac{\pi abp_o^2(\frac{\pi b}{E(e)})^2}{8\mu\, Po_c RTL} \times\left[\frac{p_i^2}{p_o^2} - 1 + 2\alpha\frac{2-\sigma}{\sigma}Kn_o\left(\frac{p_i}{p_o} - 1\right)\right] \tag{33}$$

The limit of Eq. (33) for $b/a \to 1$ reduces to circular tubes [12]:

$$\dot{m} = \frac{a^4\pi p_o^2}{16\mu\, LRT}\left[\frac{p_i^2}{p_o^2} - 1 + 16\frac{2-\sigma}{\sigma}Kn_o\left(\frac{p_i}{p_o} - 1\right)\right] \tag{34}$$

The continuum flow mass flow rate is given by:

$$\dot{m}_c = \rho\bar{u}A = \frac{\pi abp_o^2(\frac{\pi b}{E(e)})^2}{8\mu\, Po_c RTL}\left(\frac{p_i^2}{p_o^2} - 1\right) \tag{35}$$

The effect of slip may be illustrated clearly by dividing the slip flow mass flow equation (33) by the continuum mass flow equation (35)

$$\frac{\dot{m}}{\dot{m}_c} = 1 + \frac{2\alpha\frac{2-\sigma}{\sigma}Kn_o}{\frac{p_i}{p_o} + 1} \tag{36}$$

It is seen that the rarefaction increases the mass flow and that the effect of rarefaction becomes more significant when the pressure ratio decreases. By including the slip velocity at the wall, one adds another term to the mass flow equation; therefore, the mass flow rate for a given inlet and outlet pressure always increases due to the effect of slip. This could be interpreted as an apparent reduction of the fluid viscosity.

Table 2
Poiseuille number results for elliptic ducts

ε	Po			
	$Kn^* = 0$	$Kn^* = 0.01$	$Kn^* = 0.05$	$Kn^* = 0.1$
0.1	9.657	8.657	6.125	4.490
0.2	9.301	8.379	6.012	4.457
0.3	8.948	8.110	5.917	4.443
0.4	8.647	7.884	5.846	4.440
0.5	8.412	7.709	5.795	4.440
0.6	8.239	7.582	5.759	4.440
0.7	8.122	7.496	5.735	4.439
0.8	8.049	7.442	5.721	4.440
0.9	8.011	7.415	5.715	4.443
1	8.000	7.407	5.714	4.444
Eq. (30)	8.000	7.407	5.714	4.444

Combining Eqs. (32) and (33), we obtain the expression for pressure distribution:

$$\frac{p_z}{p_o} = -\alpha\frac{2-\sigma}{\sigma}Kn_o + \left(\left(\alpha\frac{2-\sigma}{\sigma}Kn_o + \frac{p_i}{p_o}\right)^2 - \left[\frac{p_i^2}{p_o^2} - 1 + 2\alpha\frac{2-\sigma}{\sigma}Kn_o\left(\frac{p_i}{p_o} - 1\right)\right]\frac{z}{L}\right)^{1/2} \tag{37}$$

4. Results and discussion

Table 1 presents a comparison of the Poiseuille number results using one to four terms of binomial series approximation respectively. For the practical application range $\varepsilon > 0.1$, taking first three terms to obtain the Poiseuille number is accurate enough. More terms should be used when aspect ratio ε is comparatively small and Knudsen number is comparatively large.

Table 2 shows the Poiseuille number results for different aspect ratio ε and Kn. The Po values decrease with an increase of Kn for the same aspect ratio. Ebert and Sparrow [13] and Sreekanth [14] also theoretically demonstrated that the rarefaction leads to a reduction of the Po for increasing Kn. The Po values decrease with an increase of ε for the same Kn. When $b/a \to 1$, the Poiseuille number results reduce to circular tubes solution equation (30).

The Poiseuille number results can be presented conveniently in terms of normalized Poiseuille number. Furthermore, the ef-

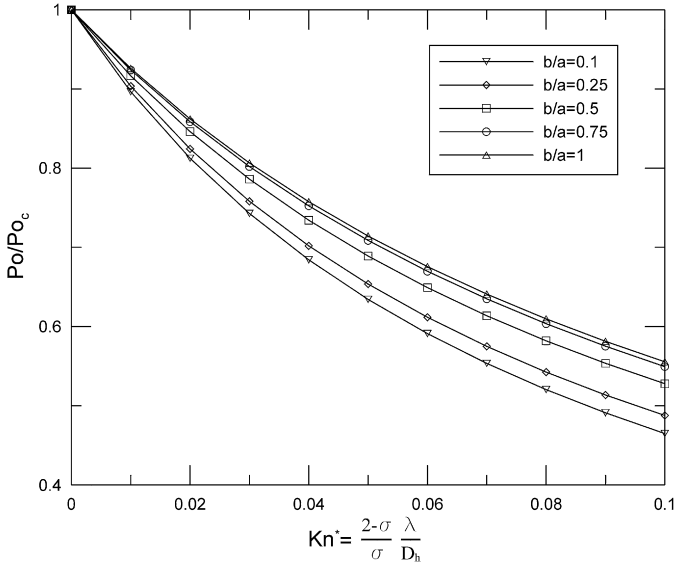

Fig. 2. Normalized *Po* results as a function of aspect ratio and *Kn* for elliptic ducts.

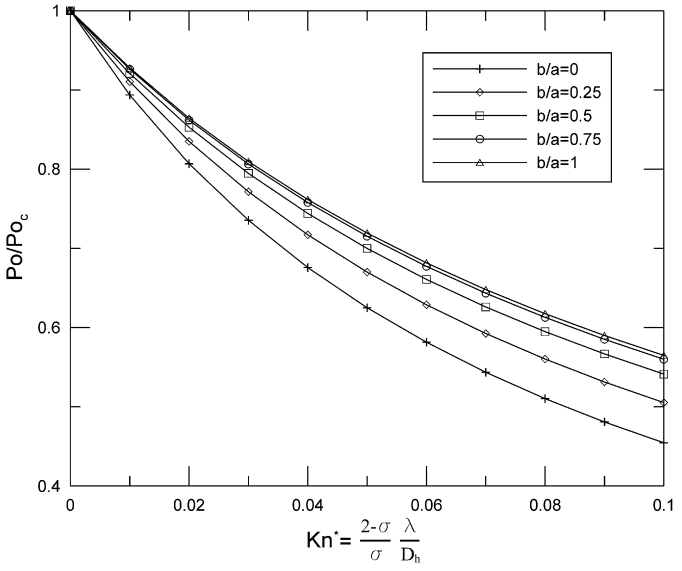

Fig. 3. Normalized *Po* results as a function of aspect ratio and *Kn* for rectangular ducts.

Table 3
The constants α for the Poiseuille number ratio

ε	α
0.1	11.522
0.15	11.242
0.2	10.911
0.25	10.556
0.3	10.196
0.4	9.531
0.5	8.989
0.6	8.587
0.75	8.211
0.85	8.076
1	8

fects of slip are illustrated clearly by plotting the ratio Po/Po_c as a function of the Knudsen number and aspect ratio, where Po_c represents the continuum flow value. Fig. 2 shows the normalized Poiseuille number results for elliptic ducts as a function of aspect ratio ε and *Kn*. From an inspection of the graphs, it is seen that *Po* decreases as the rarefaction becomes greater. Fig. 3 demonstrates the normalized Poiseuille number results for rectangular ducts as a function of aspect ratio and *Kn* [26]. It is seen that the normalized Poiseuille number results for elliptic and rectangular ducts have similar trends. A comparison has been made between the rectangular and elliptic duct solutions and the reliability of the present proposed solution has been proven. Details can be found in [26].

The Poiseuille number reduction depends on the geometry of the cross-section. It is convenient that the Poiseuille number results are expressible to good accuracy by the relation

$$\frac{Po}{Po_c} = \frac{1}{1 + \alpha \frac{2-\sigma}{\sigma} Kn} \tag{38}$$

in which α depends on the duct geometry. For other geometries, $\alpha = 12$ for the parallel plate and $\alpha = 8$ for the circular tube.

For an elliptic duct, the constants, α, are derived from a least-square fit of the Poiseuille number results (Fig. 2). It is found that the maximum error incurred by using these constants in Eq. (38) is less than 0.3%. The error is much smaller and negligible for most cases i.e. <0.05%. The constants α are listed in Table 3 and the data points are fitted to a simple correlation:

$$\alpha = 12.53 - 9.41\varepsilon + 4.87\varepsilon^2 \tag{39}$$

then

$$\frac{Po}{Po_c} = \frac{1}{1 + (12.53 - 9.41\varepsilon + 4.87\varepsilon^2)\frac{2-\sigma}{\sigma} Kn} \tag{40}$$

where $Po_c = (1 + \varepsilon^2)(\pi / E(e))^2$, see Shah and London [27].

Therefore, using the simple expression equation (40), the Poiseuille number results can be easily obtained. As a further proof of the reliability of the proposed solution, Eq. (29), all the numerical results obtained in slip flow reduce to their continuum flow limits in the limit of $Kn \to 0$ [27]. Moreover, the limit of Eq. (29) for $b/a \to 1$ corresponds to the circular tube solution.

Fig. 4 shows the pressure distribution with and without rarefaction predicted by Eq. (37) for different pressure ratios. The pressure distribution exhibits a nonlinear behavior due to the compressibility effect. The pressure drop required is less than that in a conventional channel. The deviations of the pressure distribution from the linear distribution decrease with an increase in Knudsen number. The nonlinearity increases as the pressure ratio increases. The effects of compressibility and rarefaction are opposite as Karniadakis et al. [28] demonstrated.

In the present analysis for the pressure distribution and mass flow rate, momentum changes are neglected. The effect of the momentum changes will become important when Reynolds number is increased. The effects of momentum changes on pressure distribution and mass flow rate will be discussed in detail in a future work.

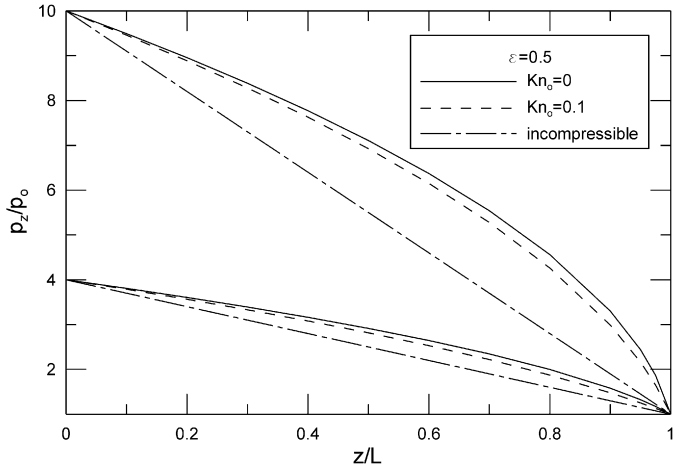

Fig. 4. The pressure distribution for different pressure ratios.

5. Conclusion

This paper investigated slip flow in elliptic microchannels. An analytical solution of Poiseuille number was obtained using separation of variables in elliptic cylinder coordinates. A simple model (Eq. (40)) was developed for predicting the Poiseuille number in elliptic microchannels for slip flow. The accuracy of the proposed simple model was found to be within 3 percent of exact values. The developed model may be used to predict mass flow rate and pressure distribution of slip flow in elliptic microchannels.

Acknowledgements

The authors acknowledge the support of the Natural Sciences and Engineering Research Council of Canada (NSERC).

References

[1] E.G.R. Eckert, R.M. Drake, Analysis of Heat and Mass Transfer, McGraw–Hill, New York, 1972, pp. 467–486.
[2] E.B. Arkilic, K.S. Breuer, M.A. Schmidt, Gaseous flow in microchannels, in: Proceedings of ASME Application of Microfabrication to Fluid Mechanics, vol. FED-197, 1994, pp. 57–66.
[3] E.B. Arkilic, K.S. Breuer, M.A. Schmidt, Gaseous slip flow in long microchannels, J. Microelectromechanical Systems 6 (1997) 167–178.
[4] J. Liu, Y.C. Tai, C.M. Ho, MEMS for pressure distribution studies of gaseous flows in microchannels, in: Proceedings of IEEE International Conference on Micro Electro Mechanical Systems, Amsterdam, Netherlands, 1995, pp. 209–215.
[5] J. Pfahler, J. Harley, H. Bau, J.N. Zemel, Gas and liquid flow in small channels, in: Proceedings of Micromechanical Sensors, Actuators, and Systems, vol. 32, ASME, 1991, pp. 49–59.
[6] J. Pfahler, J. Harley, H. Bau, J.N. Zemel, Gas and liquid transport in small channels, in: Proceedings of Microstructures, Sensors and Actuators, vol. 19, ASME, 1990, pp. 149–157.
[7] J. Harley, Y. Huang, H. Bau, J.N. Zemel, Gas flows in micro-channels, J. Fluid Mech. 284 (1995) 257–274.
[8] S.B. Choi, R.F. Barron, R.O. Warrington, Fluid flow and heat transfer in microtubes, in: Proceedings of Micromechanical Sensors, Actuators, and Systems, vol. 32, ASME, 1991, pp. 123–134.
[9] S. Wu, J. Mai, Y. Zohar, Y.C. Tai, C.M. Ho, A suspended microchannel with integrated temperature sensors for high pressure flow studies, in: Proceedings of IEEE Workshop on Micro Electro Mechanical Systems, Heidelberg, Germany, 1998, pp. 87–92.
[10] T. Araki, M.S. Kim, I. Hiroshi, K. Suzuki, An experimental investigation of gaseous flow characteristics in microchannels, in: G.P. Celata, et al. (Eds.), Proceedings of International Conference on Heat Transfer and Transport Phenomena in Microscale, Begell House, New York, USA, 2000, pp. 155–161.
[11] S.A. Schaaf, P.L. Chambre, Flow of Rarefied Gases, Princeton Univ. Press, Princeton, NJ, 1958.
[12] E.H. Kennard, Kinetic Theory of Gases, McGraw–Hill, New York, 1938.
[13] W.A. Ebert, E.M. Sparrow, Slip flow in rectangular and annular ducts, J. Basic Engrg. 87 (1965) 1018–1024.
[14] A.K. Sreekanth, Slip flow through long circular tubes, in: L. Trilling, H.Y. Wachman (Eds.), Proceedings of the Sixth International Symposium on Rarefied Gas Dynamics, Academic Press, San Diego, CA, 1969, pp. 667–680.
[15] Y. Mitsuya, Modified Reynolds equation for ultra-thin film gas lubrication using 1,5-order slip-flow model and considering surface accommodation coefficient, J. Tribol. 115 (1993) 289–294.
[16] C. Aubert, S. Colin, High-order boundary conditions for gaseous flows in rectangular microducts, Microscale Thermophysical Engrg. 5 (2001) 41–54.
[17] R.G. Deisler, An analysis of second-order slip flow and temperature-jump boundary conditions for rarefied gases, Int. J. Heat Mass Transfer 7 (1964) 681–694.
[18] S. Colin, P. Lalonde, R. Caen, Validation of a second-order slip flow model in rectangular microchannels, Heat Transfer Engrg. 25 (2004) 23–30.
[19] R.W. Barber, D.R. Emerson, Challenges in modeling gas-phase flow in microchannels: from slip to transition, Heat Transfer Engrg. 27 (2006) 3–12.
[20] P. Moon, D. Spencer, Field Theory for Engineers, Van Nostrand, Princeton Univ. Press, 1961.
[21] P. Moon, D. Spencer, Field Theory Handbook, second ed., Springer-Verlag, Berlin/New York, 1971.
[22] W.M. Rohsenow, H.Y. Choi, Heat, Mass, and Momentum Transfer, Prentice Hall Inc., New York, 1961.
[23] M. Abramowitz, I.A. Stegun, Handbook of Mathematical Functions, Courier Dover Publications, 1965.
[24] N.M. Lebedev, I.P. Skalskaya, Y.S. Uflyand, Worked Problems in Applied Mathematics, Courier Dover Publications, 1965.
[25] Maple 9, Waterloo Maple Software, Waterloo, Canada, 2003.
[26] Z.P. Duan, Y.S. Muzychka, Slip flow in non-circular microchannels, Microfluidics Nanofluidics (2006), in press, DOI 10.1007/s10404-006-0141-4.
[27] R.K. Shah, A.L. London, Laminar Flow Forced Convection in Ducts, Academic Press, San Diego, CA, 1978.
[28] G.E. Karniadakis, A. Beskok, N. Aluru, Microflows and Nanoflows, Springer-Verlag, Berlin/New York, 2005.